Comparing experiments with modeling for light ion helicon plasma sources

M. D. Carter, F. W. Baity, Jr., G. C. Barber, and R. H. Goulding
Oak Ridge National Laboratory, Oak Ridge, Tennessee 37831-8071

Y. Mori
Kyushu University, Kasuga-city, Fukuoka, Japan

D. O. Sparks, K. F. White, and E. F. Jaeger
Oak Ridge National Laboratory, Oak Ridge, Tennessee 37831-8071

F. R. Chang-Díaz and J. P. Squire
NASA Advanced Space Propulsion Laboratory, Houston, Texas 77059

(Received 24 May 2002; accepted 11 September 2002)

The ability to obtain high plasma densities with high fractional ionization using readily available, low-cost components makes the helicon a candidate plasma source for many applications, including plasma rocket propulsion, fusion component testing, and materials processing. However, operation of a helicon can be a sensitive function of the magnetic field strength and geometry as well as the driving frequency, especially when using light feedstock gases such as hydrogen or helium. In this paper, results from a coupled rf and transport model are compared with experiments in the axially inhomogeneous Mini-Radio Frequency Test Facility [Goulding *et al.*, *Proceedings of the International Conference on Electromagnetics in Advanced Applications (ICEAA 99), Torino, Italy, 1999* (Litografia Geda, Torino, 1999), p. 107] (Mini-RFTF). Experimental observations of the radial shape of the density profile can be quantitatively reproduced by iteratively converging a high-resolution rf calculation including the rf parallel electric field with a transport model using reasonable choices for the transport parameters. The experimentally observed transition into the high density helicon mode is observed in the model, appearing as a nonlinear synergism between radial diffusion, the rf coupling to parallel electric fields that damp near the plasma edge, and propagation of helicon waves that collisionally damp near the axis of the device. Power deposition from various electric field components indicates that inductive coupling and absorption in the edge region can reduce the efficiency for high-density operation. The effects of absorption near the lower hybrid resonance in the near-field region of the antenna are discussed. Ponderomotive effects are also examined and found to be significant only in very low density and edge regions of the Mini-RFTF discharge. © *2002 American Institute of Physics.* [DOI: 10.1063/1.1519539]

I. INTRODUCTION

The term ''helicon'' is often used generically to refer to a cylindrical plasma source with an axial magnetic field that is driven by radio frequency waves at frequencies between the ion and electron cyclotron frequencies. These devices are capable of producing plasma densities $\gtrsim 10^{19}$ m^{-3} with only a few kW of rf power and can ionize a large fraction of an incoming gas stream. A few of the possible applications include space propulsion,[1,2] fusion startup and component testing,[3] plasma etching and deposition for semiconductors,[4] and waste processing of hazardous chemicals.[5] The devices typically consist of a dielectric gas tube surrounded by an antenna, a vacuum pumping system, and a gas feed system. Figure 1 shows a schematic of the axially inhomogeneous Mini-Radio Frequency Test Facility (Mini-RFTF)[6] that provides the experimental results given in this paper. Helicon research in the Mini-RFTF device has been performed for several years,[6] and many recipes have been developed to obtain high-density ($>10^{18}$ m^{-3}) stable discharges in hydrogen and deuterium plasmas.

In high-density operation, the rf antenna typically drives a helicon wave with an electric field polarization corresponding to the direction of the electron gyromotion: a right-hand circularly polarized wave. This mode has a maximum perpendicular electric field component on axis corresponding to the J_0 Bessel function,[7–9] and helicon antennas are often designed to predominantly excite this $m=1$ mode. However, the $m=0$ azimuthal mode has also been used effectively to drive helicon plasmas,[10,11] and, in general, helicon operation covers a very broad range of plasma parameters involving many interrelated physical mechanisms. Not only is the final plasma state highly dependent on the system design and the operational scenario, it also depends on the rf coupling and all of the atomic interactions and transport losses in the device. Furthermore, rf coupling mechanisms are needed over a wide range of densities from startup to the final state.[11]

A nearly ubiquitous feature of helicon devices is that a power threshold exists where the mode of operation abruptly changes from a low- to a high-density (helicon) mode, and the Mini-RFTF is no exception. In many experiments, threshold power levels are observed to cause jumps in the plasma density by more than an order of magnitude with small increases in the total applied rf power. Specific ex-

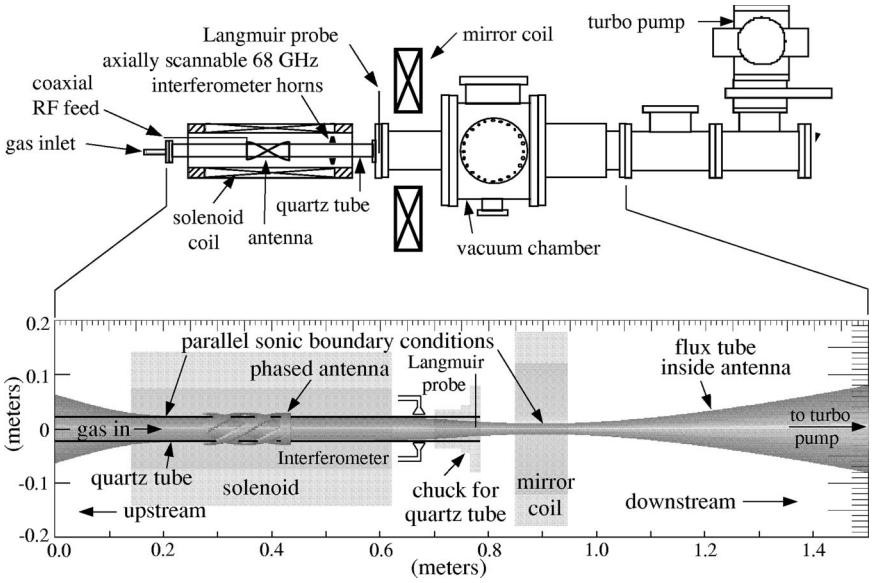

FIG. 1. A schematic of the Mini-RFTF device at ORNL with an expansion of the region that is modeled shows the vacuum configuration for the experiment and the location of the diagnostics used. The upstream and downstream directions are based on the direction of the gas flow. Transport modeling is only performed upstream of the mirror coil.

amples of these jumps are given in Refs. 12, 13, 14, and 15. Additional jumps can occur in the high-density mode of operation caused by shifts in the radial or axial eigenmode for the helicon wave.[8,10,12,16] The plasma density is highly peaked on the axis for these high-density modes of operation.

In this paper, we demonstrate that many of the operational features of the Mini-RFTF device, including the transition from low- to high-density plasma profiles, can be modeled quantitatively for hydrogen operation. A power threshold to achieve highly peaked density profiles is found in the model. A trade-off between the rf power coupled to the helicon mode and that coupled inductively near the plasma edge gives rise to a transition between low-density operation and high-density centrally peaked profiles as the power is increased. A synergism between the radial transport and the rf power deposition is ultimately responsible for the transition. Power coupled inductively to the plasma edge is required for the formation of the discharge, but this inductively coupled power can significantly reduce the overall efficiency of the discharge because of rapid losses near the edge of the device.

The cornerstone of the model is an accurate high-resolution solution to Maxwell's equations for the rf fields based on cold plasma conductivity that includes realistic antenna and static magnetic field geometries. A plasma density profile that is consistent with the rf power deposition is obtained by iterating the rf calculation with a flux-tube-averaged transport model similar to that of Ref. 17. The best agreement between the model and the experiment is obtained when the transport is based on classical diffusion.

In Sec. II, we review the general dispersion and damping mechanisms of waves in the operating regime for the Mini-RFTF experiments. In Sec. III we describe the experimental conditions, diagnostics used, and results obtained in the Mini-RFTF. Section IV discusses the iterative rf and transport model used for comparison with the experiment. The rf calculation with radially and axially varying plasma parameters is described in Sec. IV A. The transport model is described in Sec. IV B. The particle transport model along with simple estimates for the effect of magnetic mirrors on the axial plasma density distribution is given in Sec. IV B 1. A description of the power balance and the importance of considering the ionization process is given in Sec. IV B 2. Results and comparisons between the experiment and the model are given in Sec. V. Emphasis is given to (Sec. V A) radial transport scaling, (Sec. V B) power threshold for high-density operation, (Sec. V C) fractional edge deposition for high-density operation and the possible role of the lower hybrid resonance, (Sec. V D) cavity effects and loading, and (Sec. V E) ponderomotive effects. Conclusions and directions for further investigation are given in Sec. VI.

II. DISPERSION AND DAMPING MECHANISMS FOR WAVES IN HELICONS

The fast helicon dispersion relation for high-density operation was identified in early work by Chen.[18] That dispersion relation ignored ion contributions to the plasma current and restricted consideration to an rf frequency, ω, between the electron cyclotron frequency, ω_{ce}, and the lower hybrid frequency,[19] ω_{lh}, given for a two-species plasma by $\omega_{lh} \equiv [|\omega_{ci}\omega_{ce}|^{-1} + (\omega_{pi}^2 + \omega_{ci}^2)^{-1}]^{-1/2}$, where $\omega_{cj} = q_j B_0 / m_j$, is the cyclotron frequency of the jth species, $\omega_{pj} = \sqrt{q_j^2 n_j / (\epsilon_0 m_j)}$ is the plasma frequency for the jth species, B_0 is the static magnetic field strength, ϵ_0 is the permittivity of free space, and q_j, m_j, n_j denote the species charge (with sign), mass, and density of the jth species, respectively. The fast wave helicon dispersion relation was extended to include finite electron mass, and thus the Trivelpiece–Gould mode (i.e., Refs. 14 and 8), giving the dispersion relation

$$k_\parallel \sqrt{k_\parallel^2 + k_\perp^2} - \frac{\omega}{\omega_{ce}}(k_\parallel^2 + k_\perp^2) = \frac{\mu_0 n_e e \omega}{B_0} = \frac{\omega}{|\omega_{ce}|}\left(\frac{\omega_{pe}}{c}\right)^2, \tag{1}$$

where μ_0 is the permeability of free space, and the assumption that $\omega_{pe} \gg \omega$ has been made.

Note that Eq. (1) does not include any of the ion mass dependence that has been shown to play a role in light-ion helicon operation. Maximum densities in Mini-RFTF are often found when the rf frequency matches the lower hybrid resonance near the antenna[6] similar to findings by others,[20–22] and more on the effect of the lower hybrid resonance in the near-field region of the antenna will be discussed later. RF effects may also play a role through slow waves on the resonance cone during startup.[11,23] The experimentally observed ion dependence also typically leads to more difficult operation with light ions, which may be partially attributed to the increased sound speed and reduced confinement along field lines for light ions.

The damping mechanisms for high-density discharges have been debated for many years.[24] Several collisionless absorption mechanisms based on linear and nonlinear Landau damping have been proposed that usually rely on direct excitation of and/or mode conversion to electrostatic or surface modes.[24–28] However, for many operational regimes, strong decorrelation between the electron motion and the rf waves can be caused by electron–neutral collisions, Coulomb collisions, or interactions between electrons and the confining electrostatic potential in the device. The electron–neutral collision frequency is proportional to the electron speed and the neutral density. The neutral density at fixed pressure is inversely proportional to the temperature of the neutral gas inside the discharge. The neutral temperature may significantly exceed room temperature in helium discharges,[29] and could be very high for the hydrogen discharges considered here because of Franck–Condon neutrals. However, the electron–neutral collision rate can be crudely estimated using the total atomic cross section[30] at standard temperature and pressure giving ~ 1 MHz per mTorr of fill pressure for electron temperatures of interest (5–10 eV). Typical gas pressures in the Mini-RFTF device are a few tens of mTorr so that the electron–neutral collision rate can be a significant fraction of the rf frequency. The Coulomb collision frequency is $\sim 70/T_e^{3/2}$ MHz per 10^{19} m^{-3} of electron density, which for typical electron temperatures is ~ 3 MHz per 10^{19} m^{-3} of electron density. So, the Coulomb collision rate can become comparable to the neutral collision rate for very high plasma density. At a minimum, in the absence of both electron–neutral and Coulomb collisions, the bounce motion of electrons inside the electrostatic plasma potential well can lead to decorrelation on a time scale of order 0.2 MHz/L_h, where L_h is roughly the length of the system in meters. Thus, it is possible for any of these decorrelation rates to become a significant fraction of the driven rf frequency, and collisional decorrelation typically cannot be ignored. These collisional processes also result in significantly more dissipation than can typically be explained by linear or nonlinear Landau damping mechanisms,[25] although the precise damping mechanism may depend on the parameter regime of operation. Thus, for high-density operation ($\gtrsim 5 \times 10^{18}$ m^{-3}), where slow waves are nonexistent or damped over a very short distance and where the collision rate is a significant fraction of the driven rf frequency, collisional damping and focusing of the fast (helicon) wave on the axis must play an important role, as will be shown in Sec. V.

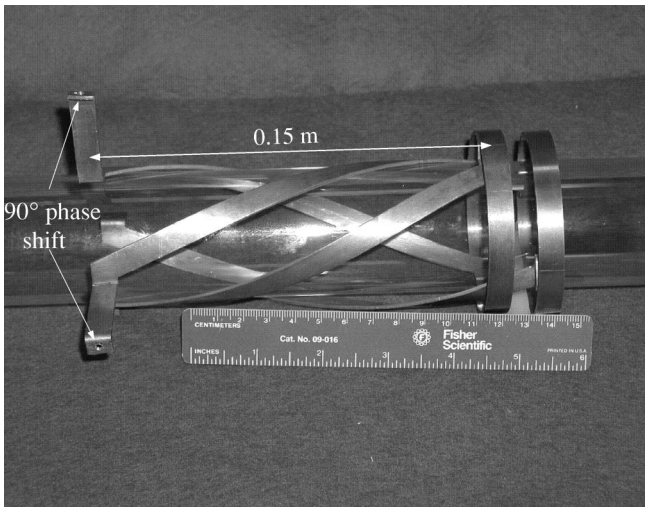

FIG. 2. A quad-phased antenna with 90° phasing between helical segments was used for most of the experiments and the modeling described in this paper.

III. MINI-RFTF EXPERIMENTAL SETUP AND OBSERVATIONS

A schematic of the Mini-RFTF facility is shown in Fig. 1. The device consists of a 48 cm long solenoid magnet capable of a maximum field of 0.4 T (using the present power supplies), with a 14 cm bore, in which the 5 cm diameter quartz helicon source tube is centered (Fig. 1). The solenoid magnet has six radial layers with 28 windings per layer for a total of 168 turns. The source tube feeds into a vacuum chamber with two mirror coils; however, only the mirror coil closest to the solenoid was energized for the work presented here. The mirror coils have five radial layers with eight windings per layer, giving a total of 40 turns. An end-mounted turbo-pump produces a background pressure of 2×10^{-7} Torr. The device can be operated at steady state or pulsed. It features a flexible geometry antenna bolted into a ground plane. Parts of the antenna can easily be exchanged to allow for geometry changes. Diagnostics include a 68 GHz interferrometer that can be axially scanned, and a Langmuir probe that allows full radial measurements. Data are obtained by using a LabVIEW-based data acquisition system running on a PC. Gas-handling and safety systems have been designed to permit hydrogen operation.

The antenna used for most of the data presented here is a phased dual design as shown in Fig. 2. It is ~ 0.15 m in length, with four helical current carriers having 90° relative phasing to excite a nearly pure $m=1$ spectrum. Two amplifiers were used with a 90° phase delay to drive the quad antenna shown in Fig. 2. Mutual coupling between the phased segments was minimized in the design, but an additional inductor was used between the matching circuits for each amplifier to decouple the circuits. Total powers of up to 2 kW were delivered with typical operation at 1800 W. The power to the plasma was measured in the experiment by first measuring the vacuum loading and determining that it was small compared to loading with plasma. The power coupled to the plasma is estimated by subtracting reflected from forward power with the reflected power tuned to typically less

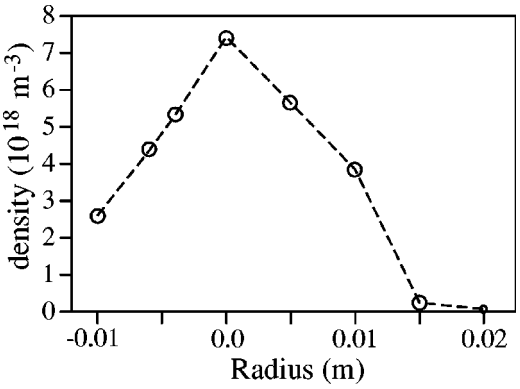

FIG. 3. The Langmuir probe (see Fig. 1) measures a typical radial electron density profile that is highly peaked. For this case, 2500 W of rf power was delivered to the plasma. The mirror coil current was 1000 A while the solenoid coil carried 55 A giving a magnetic field strength under the antenna of roughly 0.025 T under the antenna. Deuterium with a gas flow rate of 92 sccm was used giving a pressure of ~12 mTorr downstream. The circle size indicates the shot-to-shot variation over 2 to 4 shots.

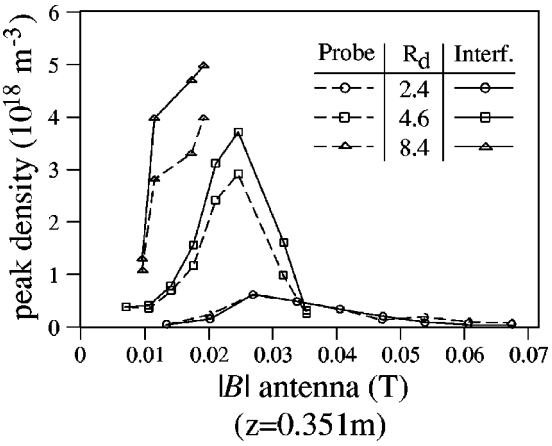

FIG. 4. The hydrogen plasma parameters obtained using a quadrapole antenna in Mini-RFTF show a strong dependence on mirror ratio and the magnetic field near the helicon antenna. Power delivered to the plasma was ~1800 W at 16 MHz in all cases. The lower hybrid resonance appears in the antenna region for all magnetic field strengths $\gtrsim 0.0245$ T.

than one tenth the forward power in the final plasma state. A current and voltage sensor placed between the match box and the antenna has also been used to confirm that typically $\gtrsim 90\%$ of the power is coupled to the plasma. The current and voltage sensor is easily destroyed so it was not typically used in the data presented here. Phase and amplitude detectors were used to monitor the rf antenna so that power was balanced between the two phased segments to within 20%.

As shown in Fig. 3, highly peaked density profiles are typically observed for light-gas discharges in Mini-RFTF above the power threshold for the helicon mode of operation. To produce the highest densities at fixed rf power, optimum values of the magnetic field near the antenna are chosen such that $\omega \gtrsim \omega_{lh}$ in Mini-RFTF. Optimization of plasma production with a driving frequency near the lower hybrid frequency has also been observed by several researchers.[20,22,27,13] However, the precise effects attributed to the lower hybrid resonance are complicated by the axial inhomogeneity and transport in Mini-RFTF. For example, more than one peak in density is observed as the lower hybrid resonance is swept through the antenna region. Thus, a careful investigation of the role of the lower hybrid resonance remains in progress on the Mini-RFTF device, and modeling indicates that the presence of the lower hybrid resonance in the near field region of the antenna increases edge power deposition, thereby reducing coupling to the centrally damped helicon mode. More information on lower hybrid resonance effects are given later in the paper, and the topic is still under investigation in both the experiment and model.

The range of magnetic field strengths over which reasonably high-density plasmas can be achieved is relatively narrow. The performance is also a strong function of the ratio of the magnetic fields in the mirror throat to those under the antenna, R_d, as shown in Fig. 4. Low frequency instabilities can lead to a gradual decline in density with increasing magnetic field;[31] however, no such instabilities are observed in the discharges shown here, possibly because of the magnetic field inhomogeneity and the relatively low magnetic field operation. Rather, the very sudden drop in density above a prescribed magnetic field appears to be correlated, as shown in the later modeling results, with an increase in the power threshold for accessing the high-density helicon mode of operation. Below this threshold, hollow discharges can occur in Mini-RFTF depending on the neutral collisionality, similar to those reported by Balkey.[20] The modeling results also indicate that low magnetic field operation has a lower power threshold, but that the density in the high-density helicon mode is limited by classical radial diffusion.

In contrast to the hydrogen results, high-density helium plasmas ($n_e > 10^{19}$ m^{-3}) have been produced in the Mini-RFTF,[6] and by others,[15,11,31] at high values of static magnetic field, B, for which $\omega \ll \omega_{lh}$. This regime has not been well explored in helicon sources, and it is desirable, for some applications, to replicate the high $|B|$ helicon operation with hydrogen. Additional experimental and modeling efforts with regard to the mass dependence will be performed in future work, and our focus for this paper will be on the hydrogen results.

IV. MODELING FOR AXIALLY VARYING SYSTEMS

The modeling of the experiment is performed by iterating between an high-resolution rf calculation and a transport model based on the power deposition given by the rf calculation. We describe the rf calculation in Sec. IV A and the transport model in Sec. IV B.

A. RF modeling

Maxwell's equations for the linearized cold plasma response can be written as[19]

$$\nabla \times \vec{E} = i\omega \vec{B}, \quad \nabla \times \vec{B} = \mu_0 \vec{J}_{\text{ext}} - i\omega \epsilon_0 \mu_0 \tilde{K} \cdot \vec{E},$$
$$\tilde{K} = \begin{pmatrix} S & -iD & 0 \\ iD & S & 0 \\ 0 & 0 & P \end{pmatrix}, \quad \vec{E} = (E_{\perp 1}, E_{\perp 2}, E_{\parallel}), \tag{2}$$

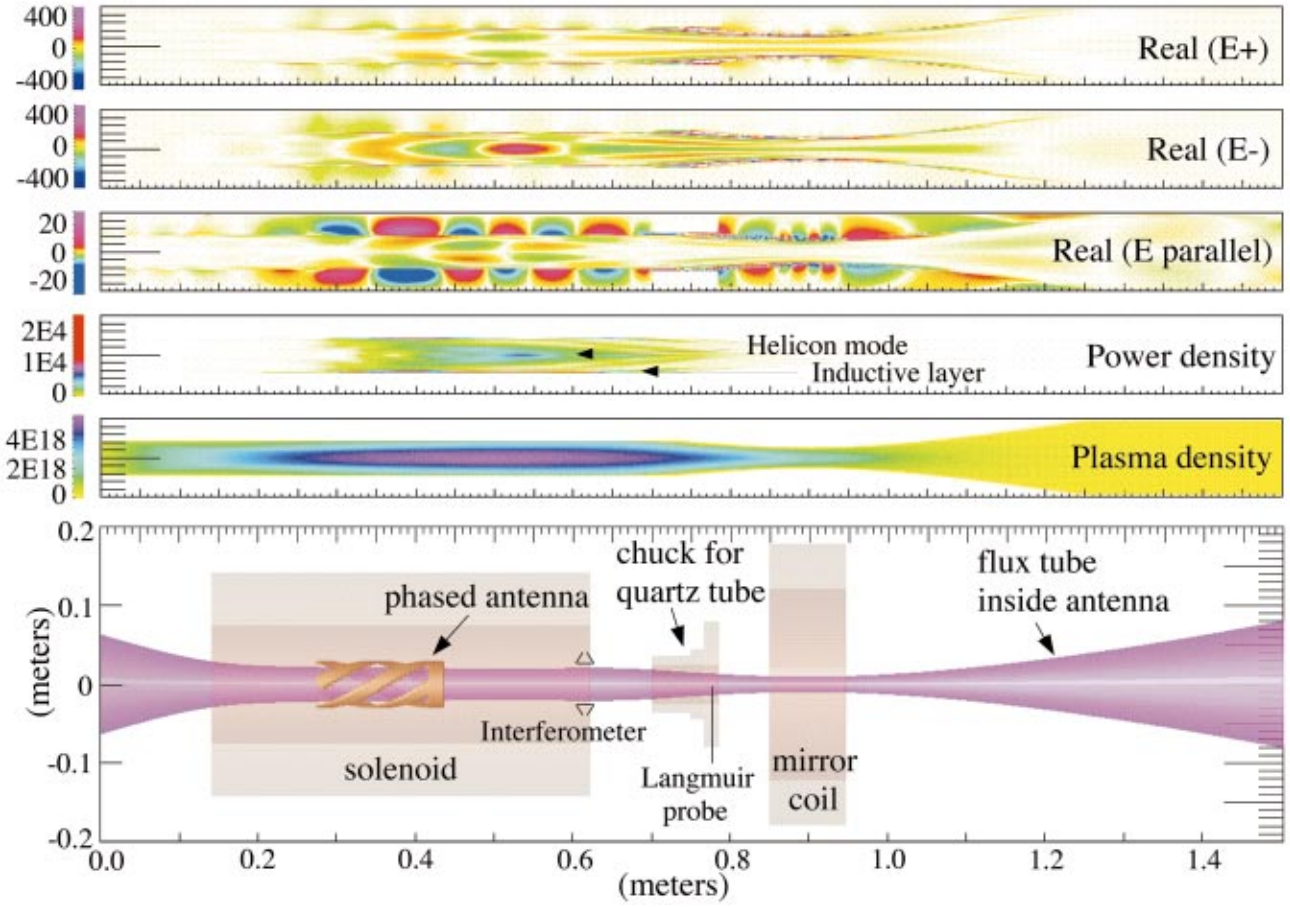

FIG. 5. (Color) The model parameters used to simulate the experiment with roughly 0.0250 T under the antenna and 0.11 T under the mirror coil (700 A in mirror coil, 56 A in solenoid). The rf frequency was taken to be 16 MHz. The density was obtained by iterating the rf and transport calculations to convergence for 2 kW of rf power. All units are in MKS. The field values are normalize to 1 A (peak in time) in each helical segment of the antenna.

where $P=1-\Sigma_j(\omega_{pj}^2/\omega^2)$, $S=1-\Sigma_j\omega_{pj}^2/(\omega^2-\omega_{cj}^2)$, and $D=\Sigma_j(\omega_{cj}/\omega)\cdot\omega_{pj}^2/(\omega^2-\omega_{cj}^2)$ describes the Hall contribution to the plasma current. In these equations, $\vec{E}$ and $\vec{B}$ are the complex rf electric and magnetic field vectors, respectively, with implicit $\exp(-i\omega t)$ time dependence, and $\vec{J}_{\text{ext}}$ represents rf current sources from the antenna; all units are MKS. The $\perp 1$ and $\perp 2$ directions are orthogonal and are perpendicular to the direction of the static magnetic field. The $\parallel$ direction is that of the static magnetic field.

The rf modeling here uses a new code, EMIR3, that retains finite $\vec{E}_\parallel$, and therefore the slow wave, to solve Eq. (2) in cylindrical coordinates. EMIR3 uses a staggered computational grid that remains accurate in both vacuum and plasma regions. Perfectly conducting boundary conditions are implemented at support structures inside the computation domain to reduce the condition number of the matrix. Regularity of the solution is enforced on the axis. The effects caused by radial feed currents for the antenna are included. Cases retaining finite $\vec{E}_\parallel$ are computationally demanding because very-short-wavelength electrostatic modes at the lower hybrid resonance must be resolved accurately to obtain good numerical solutions.

The rf fields are expanded in a periodic Fourier sum in the azimuthal coordinate, θ $(=\perp 2)$, to reduce the three-dimensional field problem to a sum over two-dimensional solutions weighted by the Fourier spectrum of the antenna. Absorption is introduced in the cold plasma model by adding an imaginary collision frequency to the RF frequency. The helical shape of the antenna is input to the code by considering rectangular strips of current spiraling on a constant r surface. For the calculations presented here, the current along the strip is assumed to be constant $(\nabla\cdot\vec{J}_{\text{ext}}=0)$, ignoring any direct capacitive coupling. (Note that electrostatic modes in the plasma can still be excited because of inhomogeneities in the antenna and the plasma.) The rf calculations for all results presented here used 130 radial and 1200 axial grid locations to resolve short wavelength surface modes near the lower hybrid resonance. Typical results for the various field polarizations and power deposition are shown in Fig. 5.

B. Transport modeling

To obtain a self-consistent plasma density profile, we use a flux-tube-averaged power balance with a particle balance in which the plasma source rate is determined from the deposited rf power, similar to work by Yasaka.[17] Diagnostics in the EMIR3 code allow the deposited power density to be calculated on radially concentric flux tubes upstream of the magnetic field maximum. This information is then used in the

transport model described below and iteratively fed back into the EMIR3 code to recalculate the rf fields with the updated plasma density.

The transport model assumes that power deposited axially upstream (see Fig. 1) of the maximum magnetic field is rapidly carried by parallel thermal conduction along field lines upstream on the flux tube. The plasma flowing downstream of the magnetic field maximum is assumed to expand rapidly without contributing significantly to the source. Note that, with the inclusion of $E_\parallel$ in the rf model, little power deposition has been observed downstream of the mirror location, contrary to results obtained when $E_\parallel$ was neglected,[32] so that the effect of power deposition downstream of the mirror throat is insignificant for the cases presented here.

1. Particle transport

Using a single fluid treatment for the steady state plasma density, n, we assume that ambipolarity is handled primarily along field lines, so that any radial currents are relaxed by field line connections at the ends. Such a diffusion model takes the following form:

$$\mathcal{S}(\psi,s)\approx -\frac{\partial}{\partial s}D_\parallel\frac{\partial n(\psi,s)}{\partial s}-\frac{\partial}{\partial \psi}D_\psi\frac{\partial n(\psi,s)}{\partial \psi}, \tag{3}$$

where $\mathcal{S}(\psi,s)$ is the local source rate, $D_\parallel$ is the collisional parallel diffusion coefficient for weakly ionized plasma,[30] D_ψ is the perpendicular diffusion coefficient, ψ is the flux tube label, and s is the distance along a field line.

The plasma source is a complicated function of electron temperature and density as well as the densities of any neutral species in the device. These quantities are not well known spatially and are very difficult to model. However, a robust model can be obtained by averaging the source over a magnetic flux tube, $\mathcal{S}(\psi,s)\rightarrow\mathcal{S}(\psi)$, and assuming the source rate on a flux tube is proportional to the total rf power deposited on that tube. Such a model provides the average value for the electron density on a flux tube and allows parameterization of the density along a field line that is consistent with the flux tube average. For a uniform geometry, separation of variables indicates a parabolic shape for the density distribution along a field line if $D_\parallel$ is independent of s. Assuming $D_\parallel$ is weakly dependent on s, one can consider a flux tube average by using

$$n(\psi,s)\approx a(\psi)s^2+b(\psi)s+N_u(\psi), \tag{4}$$

where N_u is the density at the upstream boundary of a field line. The axial fitting parameters for the density dependence along the field line, a and b in Eq. (4), are determined by the boundary conditions at each end of a field line. In a ''long–thin'' approximation, the density evolution follows:

$$\mathcal{S}(\psi)\approx C_s(\phi)\langle n\rangle/L_{\text{eff}}-4\pi\frac{\partial}{\partial\psi}\langle B_z(z)D_{rr}\rangle\psi\frac{\partial\langle n\rangle}{\partial\psi}, \tag{5}$$

where $\langle n\rangle$ is the average plasma density on the flux tube, $\psi\approx\pi r^2B_z(z)$ is the magnetic flux label, $\mathcal{S}$ is the ionization source rate, D_{rr} is the radial diffusion coefficient, C_s is the sound speed, and L_{eff} is the effective confinement length of the flux tube, including any mirror or collisionally enhanced confinement effects.

L_{eff} can be determined by the loss rates at each end of a flux tube. For mirror-constricted sonic flow at the ends,

$$\left[D_\parallel\frac{\partial n}{\partial z}\right]_{z_d}=-\frac{C_sN_d}{\sqrt{R_d}},\quad \left[D_\parallel\frac{\partial n}{\partial z}\right]_0=\frac{C_sN_u}{\sqrt{R_u}}, \tag{6}$$

gives

$$L_{\text{eff}}=\frac{z_d}{2}\left[\frac{2\sqrt{R_uR_d}+2\alpha(\sqrt{R_u}+\sqrt{R_d})/3+\alpha^2/6}{\sqrt{R_u}+\sqrt{R_d}+\alpha}\right], \tag{7}$$

where the upstream mirror has a mirror ratio of R_u, and the downstream mirror has a mirror ratio of R_d. Mirror ratios are determined from the midpoint between the boundary condition locations on a field line. The densities, N_d and N_u, in Eqs. (6) and (7) are located, respectively, at the upstream $(z=0)$ and downstream $(z=z_d)$ locations for each field line. The parameter $\alpha\equiv z_d/2\lambda_e$ is the ratio of half the distance along a field line to the electron collisional mean free path, λ_e.

The parabolic axial approximation with mirror-restricted sonic losses at each end has implications for applications that require tailoring of the axial density profile. One implication is that the maximum density along a field line can be shifted toward the end of the device having the highest mirror ratio. The axial location of the maximum density along a field line, z_m, is given by

$$z_m=\left(\frac{z_d}{2}\right)\frac{2\sqrt{R_d}+\alpha}{\sqrt{R_d}+\alpha+\sqrt{R_u}}. \tag{8}$$

Thus, for highly collisional systems where $\alpha\gg\sqrt{R_u},\sqrt{R_d}$, the maximum density along a field line remains nearly centered between the sonic boundary points, regardless of the mirror ratios. To move the maximum density closer to the downstream mirror location, as desired for some applications, the model indicates that operation should be done with $\sqrt{R_d}\gtrsim\alpha$ and $R_u=0$ (an upstream cusp). However, the average density on a flux tube may also be reduced if α becomes too low, as shown in Eq. (7), because of reduced axial collisional confinement. The density at the downstream sonic boundary (taken to be the mirror choke location in the simulations), N_d, given by

$$N_d=\frac{\langle n\rangle\sqrt{R_d}(\alpha+2\sqrt{R_u})}{2\sqrt{R_uR_d}+2\alpha(\sqrt{R_u}+\sqrt{R_d})/3+\alpha^2/6}, \tag{9}$$

is proportional to $\sqrt{R_d}$ for fixed average density on a field line. However, another implication of the model is that the ratio of the downstream particle flux, Γ_d, to the upstream particle flux, Γ_u, per Eq. (6), is

$$\frac{\Gamma_d}{\Gamma_u}=\frac{\alpha+2\sqrt{R_u}}{\alpha+2\sqrt{R_d}}. \tag{10}$$

Thus, $R_u>R_d$ is required for $\Gamma_d>\Gamma_u$, and the fluxes become nearly equal in the collisional limit, $\alpha\gg2\sqrt{R_u},2\sqrt{R_d}$.

2. Power transport

A power balance is required to complete the particle conservation equation. Rather than attempting to solve for the electron temperature or distribution function, we choose a simple power balance on a flux tube to complete the system:

$$P_{\mathrm{rf}}(\psi) = P_i(\psi) + P_{\mathrm{axial}}(\psi) + P_{\mathrm{radial}}(\psi), \tag{11}$$

where P_{rf} is the rf power delivered to the plasma, P_i is the power lost through electron–neutral collisions during the ionization process, P_{axial} is the power lost axially along field lines, and P_{radial} is the power caused by radial diffusion of plasma into or out of the flux tube. For the ionization model, we assume a fixed energy cost per electron/ion pair, E_i, so that $\mathcal{S} = P_i/E_i$. For thermalized electron distributions with temperature, T_e, that is a significant fraction of the hydrogen ionization potential, $E_i \gtrsim 36$ eV.[33,34] However, E_i is sensitive to the electron energy distribution, and could significantly exceed 36 eV for low values of T_e. Note that the value of E_i only represents the ionization potential and radiative and dissociative losses; it does not indicate the overall efficiency for ionization in the device. For axial losses, we assume $P_{\mathrm{axial}} \approx \phi C_s \langle n \rangle(\psi)/L_{\mathrm{eff}}$, where ϕ is the electrostatic potential of the flux tube. For radial power redistribution caused by diffusion, we assume

$$P_{\mathrm{radial}} = -4\pi \frac{\partial}{\partial \psi} \phi \langle B_z(z) D_{rr} \rangle \psi \frac{\partial N}{\partial \psi}.$$

With these definitions, Eqs. (5) and (11) give a closed equation for the plasma density

$$\frac{P_{rf}(\psi)}{E_i} \approx C_s(\phi) N(\psi)(1 + \phi/E_i)/L_{\mathrm{eff}} - 4\pi \frac{\partial}{\partial \psi} \langle B_z(z) D_{rr} \rangle (1 + \phi/E_i) \psi \frac{\partial N}{\partial \psi}. \tag{12}$$

Multiplying Eq. (12) through by E_i explicitly demonstrates the power balance for the system and provides physical insight for the rf power losses,

$$P_{\mathrm{rf}}(\psi) \approx C_s(\phi) N(\psi)(E_i + \phi)/L_{\mathrm{eff}} - 4\pi \frac{\partial}{\partial \psi} \langle B_z(z) D_{rr} \rangle \times (E_i + \phi) \psi \frac{\partial N}{\partial \psi}. \tag{13}$$

Terms proportional to E_i in Eq. (13) represent the power required to ionize the neutral gas. Terms proportional to ϕ represent power lost because of the kinetic energy carried by ions as they fall through the electrostatic potential. Typically for Mini-RFTF, $\phi \sim T_e$ is much less than $E_i \gtrsim 36$ eV, and one observes that the power balance is dominated by the ionization process rather than the kinetic energy of the escaping plasma. Simple estimates indicate the ultimate fate of the total rf power. As a hydrogen ion leaves the system, each ion carries its ionization potential, 13.6 eV, plus a small amount of energy, ~ 2 eV, required to dissociate the original H_2 molecule, plus its kinetic energy, $\sim \phi$, so that $(13.6\ \mathrm{eV} + 2\ \mathrm{eV} + \phi)/(E_i + \phi) \lesssim 50\%$ of the power is carried with escaping ions. This energy will ultimately appear at any location of the device where atomic and molecular recombination occur. The remaining $\gtrsim 50\%$ of the rf power, $(E_i - 13.6\ \mathrm{eV} - 2\ \mathrm{eV})/(E_i + \phi)$, is lost to radiation processes during inelastic collisions between electrons and neutral atoms or molecules. The ultimate fate of these radiated photons depends upon the materials in the system. Most of the radiated power is likely to be lost to absorbing structures or transparent apertures in the Mini-RFTF.

In greater detail specific to the computer modeling, field lines intercept a solid boundary multiple times for some magnetic geometries, preventing a consistent radial boundary condition for Eq. (12) over the entire length of the flux tube. Rigorously, a fully two-dimensional transport model, as given by Eq. (3), is required for these re-entrant flux tubes, and for any conditions where the radial losses begin to dominate the axial losses. But, the insight offered by the parabolic model helps to shed light on the effects of the axial inhomogeneity of the magnetic field on density, and in any case, the density drops over a short radial scale length where the outer flux tubes have very short magnetic field connection lengths.

In the computer model, the upstream field-line termination points are found along the ceramic (quartz) tube and along any conducting boundaries in the vacuum system. The downstream boundary condition is specified near the maximum downstream magnetic field location. The parabolic model is applied along each field line based on the flux-tube-averaged density. Inconsistencies near the boundary layer where field lines terminate upstream near the antenna are ignored because they can only be properly handled in a fully two-dimensional transport model. However, these inconsistencies appear to have only modest implications for the Mini-RFTF magnetic geometries considered here and are handled in the code by truncating the density in the region radially outside the ceramic tube.

Numerical evaluation of the flux-tube-averaged quantities are obtained by discretizing ψ and by numerically mapping the cylindrical computational grid onto the ψ grid. Eq. (12) is then solved numerically for an initial density profile and is iterated to convergence by using the RF results from the previous EMIR3 calculation to calculate a new density profile based on Eq. (12). The axial dependence that maintains the flux tube average is then applied. Transport parameters in Eq. (12) are estimated with the formulas found in Ref. 30.

The total power delivered by the transmitter must be reduced by the parasitic power lost in the rf circuit including the antenna, P_c. Considering the frequency dependence caused by the finite skin depth in the conductor, $P_c \approx (1/2) C_c \sqrt{f_{\mathrm{MHz}}}\, I_{\mathrm{rf}}^2$, with f_{MHz} the driven rf frequency in megahertz. C_c is estimated from the experimental setup to be between 0.015 and 0.03 $\Omega/\mathrm{MHz}^{1/2}$ for the Mini-RFTF circuit used for these comparisons. Plasma loadings for typical operation in the Mini-RFTF range from ~ 0.5 to 2Ω. Thus, for all of the comparisons presented in this paper, the loading is sufficient to provide a good match to the plasma, and losses to the circuit are negligible.

The presheath potential along a field line is strongly influenced by collisionality, the source rate, and the flux tube

average of the electron temperature. It may be further complicated by the ponderomotive force in some regimes. A complete modeling including the electron distribution is beyond the scope of the model here. Rather, we seek to isolate important physical effects, so we assume the flux tube potential in Eq. (12) is given by

$$\phi \approx T_e + \alpha_p \phi_p(\psi), \tag{14}$$

where ϕ_p is the flux tube averaged ponderomotive potential estimated from the parallel rf electric field calculation, T_e, assumed constant, is proportional to the electron temperature, and $\alpha_p < 1$ is a free parameter in the model. The EMIR3 diagnostic generates an estimate for the maximum ponderomotive potential (in volts) by using a simple approximation that is reasonable far from the ion cyclotron frequency,

$$\phi_p \approx \frac{e|E_\parallel|^2}{4m_e\omega^2} \approx 4.4\times 10^{10}|E_\parallel|^2(\psi)/\omega^2, \tag{15}$$

where $|E_\parallel|^2(\psi)$ is taken to be the θ average of the maximum value of the parallel electric field along a field line within the upstream range of the flux tube. With such a model, we can vary α_p between zero and one to compare results based on no ponderomotive effect with results having the largest possible ponderomotive effect.

V. COMPARISON BETWEEN MODEL AND EXPERIMENT

The magnetic field parameters for the Mini-RFTF device are calculated accurately in the EMIR3 model by using a coil filament model. The quadrupole rf antenna is modeled with a single azimuthal Fourier mode because the phased antenna structure is effective at isolating this wave. Parameters for the transport model are taken by following field lines and by performing flux surface averages. Field lines that terminate at more than two locations along the system are not dealt with individually; rather, they are folded into the average, as discussed in Sec. IV. In Fig. 6, the model results are overlaid with experimental results from Fig. 4. Over the range of parameters studied, reasonable agreement is found between the final density state in the model and the experiment when we use classical electron radial diffusion (described below) and axial collisional confinement that is enhanced by magnetic mirror effects. Typical results from the model for the waves, the final density profile, and the power deposition, found above the power threshold are shown in Fig. 5. Note the focusing effect on fields from the helicon mode near $z = 0.5$ m.

In the remainder of this section we discuss how classical radial diffusion gives the best agreement with the experimental results, and possible shortcomings in the transport model in Sec. V A. The power threshold for high density operation and the formation of hollow radial density profiles at high magnetic fields is shown in Sec. V B. The effect of rf power deposition in the edge on the efficiency of the device, and the possible role of the lower hybrid resonance is discussed in Sec. V C. A qualitative comparison of the antenna loading and the reasons for an absence of significant cavity effects in both the experiment and the model are given in Sec. V D.

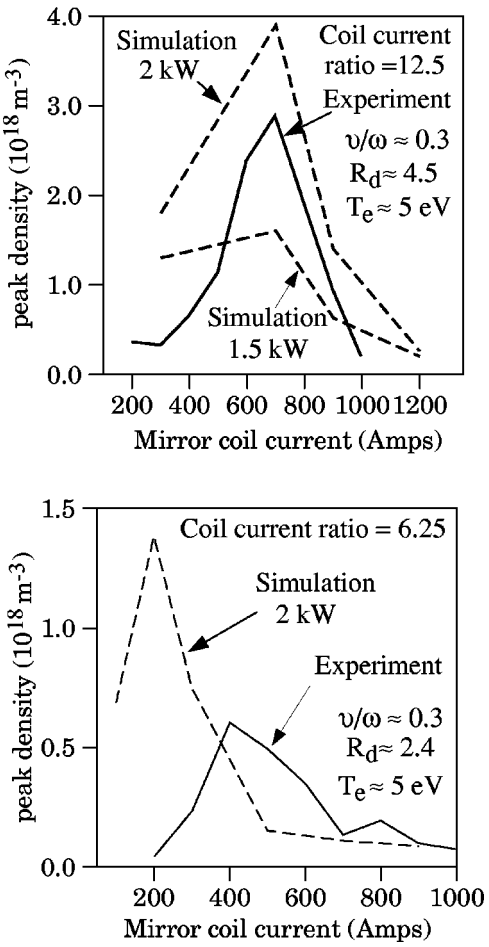

FIG. 6. EMIR3 modeling results based on classical diffusion give reasonable agreement with experimental results from Fig. 4. An electron temperature of 5 eV was used for all simulations. A drop in the electron temperature caused by enhanced radial losses, with a resulting increase in radiation losses, may explain the discrepancy for the low magnetic field cases.

Ponderomotive effects and the possibility of generating a very small population of high energy ions in the downstream halo plasma is discussed in Sec. V E.

A. Radial transport scaling

For radial diffusion, two scalings for $\langle B_z(z)D_{rr}\rangle$ were compared with experimental results. One scaling was for Bohm diffusion where $\langle B_z(z)D_{rr}^{\mathrm{Bohm}}\rangle \approx 0.06T_e$ Tm^2/s, with T_e in electron volts, is independent of the magnetic field, depending only on the electron temperature. The other scaling was for classical electron diffusion based on the total electron collision frequency, ν_e, such that $\langle B_z(z)D_{rr}^{\mathrm{Class}}\rangle \approx \langle \nu_e B\rho_e^2/2\rangle \approx 3\times 10^{-12}T_e\langle \nu_e/B\rangle$Tm^2/s with T_e in electron volts and B in Tesla. For the comparison with experimental results, we found that classical electron diffusion gives the best fit to the experimental results and that Bohm diffusion is nearly an order of magnitude too large to explain the highest density discharges that are observed.

The model with classical diffusion for the radial electron transport matches the experimental data reasonably well for high magnetic fields for downstream mirror ratios of both $R_d \approx 4.5$ and $R_d \approx 2.4$ (Fig. 6). However, the classical diffusion model tends to over-predict the density for lower mag-

netic field cases, especially for the case with the lower mirror ratio of 2.4 shown by the experimental results in Fig. 6. The most apparent shortcomings of the flux-tube-averaged model used in this paper are the lack of self-consistent models for the electron temperature and the neutral density, but other effects could play a role. The exploration into the cause of this discrepancy remains for future work, but the following are likely candidates.

(1) The neutral gas distribution, and the resulting collision rate, may vary significantly with plasma density for fixed input power.

(2) The mismatch between the flux tube and the quartz tube, especially for $R_d \approx 2.4$, may require a fully two-dimensional transport mode to accurately account for inductive coupling and rapid transport near the edge of the plasma. The two-dimensional effects can become important when the radial losses begin to dominate the axial losses.

(3) Enhanced radial losses at low magnetic fields could lower the electron temperature, thereby increasing the radiation losses and requiring an increase in E_i in the model. Any such additional radiation losses would directly reduce the plasma source rate in the model.

(4) The ion gyroradius can become a significant fraction of the plasma radius at very low magnetic fields and can influence the confinement by changing the mechanisms for maintaining ambipolarity.

If instabilities are present, they would also require consideration in the transport model, although instabilities are not observed for the data presented here.

B. Power threshold for high-density operation

The iterative model described here tends to form two types of steady-state density profiles, depending on the total rf power delivered to the plasma. One type has relatively low plasma densities that are either hollow at relatively high magnetic field strengths, or nearly uniform in the radial direction at relatively low magnetic fields where radial losses dominate the entire discharge. The other profile, consistent with the helicon mode, has high density with a radial profile that is very peaked on axis. A transition between these two types of profiles occurs above a threshold power. In Fig. 7 we show the profiles obtained as the power level increases for different magnetic field strengths at fixed magnetic geometry (downstream mirror ration of $R_d \approx 4.5$). The power threshold increases with increasing magnetic field strength, and no transition is found below 10 kW for a modeling case with 1200 A in the mirror coil and 96 A in the solenoid, which corresponds to a magnetic field near the antenna of about 0.04 T.

The experimental measurements to directly verify a mechanism for the power threshold to achieve highly peaked density profiles are not available. However, the mechanism for this transition is clearly shown in the model. Figure 8 shows the flux-tube-averaged power density as a function of $\sqrt{\psi}$ to indicate the radial dependence of the power deposition. As shown in Fig. 8 (note the logarithmic scale), when the plasma density and coupled power are low (i.e., 0.5 kW), most of the power is deposited in the edge of the discharge

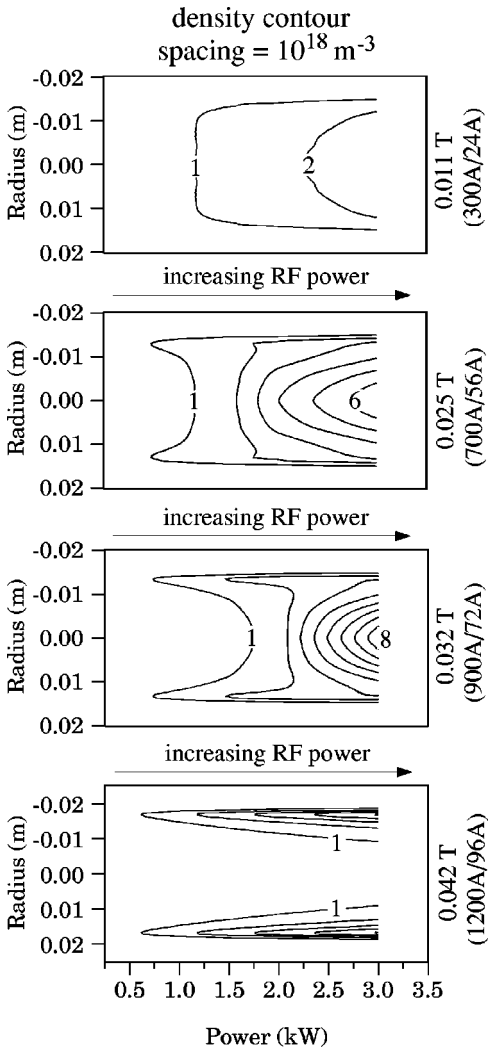

FIG. 7. Radial density profiles at the axial Langmuir probe location (see Fig. 1) are plotted versus coupled rf power to form density contours illustrating the power threshold. For the three cases with magnetic fields near the antenna of 0.011 T, 0.025 T, and 0.032 T, the density profiles at the probe change from hollow for low powers on the left side of the plot, to highly peaked as the rf power increases toward the right. For the highest magnetic field case with 0.042 T near the antenna, no peaked profiles are found over the range of power shown. Thus, the power threshold for achieving the helicon mode of operation increases sharply with increasing magnetic field for fixed magnetic geometry because axial confinement begins to dominate the radial transport. The cases shown here model a range of power levels for conditions that otherwise match the experimental setup used for $R_d = 4.5$ shown in Fig. 6.

($\sqrt{\psi} \approx 0.006$) through inductive coupling. This inductively coupled power deposited at the edge is relatively inefficient as a plasma source because rapid transport in this region can occur both radially and along field lines with short connection lengths in the edge. However, plasma can diffuse radially inward from this edge localized source to begin filling the central region of the discharge. As the power increases, the density rises, the plasma screens the evanescent modes into a narrow radial layer, and the plasma diffuses radially inward until a fast helicon mode begins to propagate. This fast helicon wave can then couple power through collisional-damping mechanisms near the axis of the plasma where confinement is good. Further increases in power raise the density

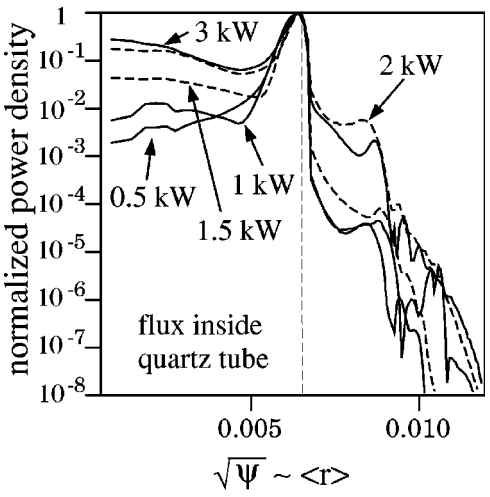

FIG. 8. The normalized power density shows the transition from inductive heating at the edge to central heating by the helicon mode as the power is increased.

and power deposition on axis until the radial density gradients become inward everywhere across the plasma. At that power and density combination, radial diffusion at the edge exhausts plasma from the region, steepening the profile at the edge and causing a transition to a highly peaked density profile above the power threshold. Thus, a factor of six change in the rf power from 0.5 kW to 3 kW increases the central power density by roughly two orders of magnitude.

C. Fractional edge deposition for high-density operation

The fraction of the power deposited by perpendicular plasma currents inside a given radius is calculated by $1-\int_\theta\int_z\int_0^r E_\parallel J_\parallel r\,dr\,dz\,d\theta/\int_\theta\int_z\int_0^r \vec{E}\cdot\vec{J}r\,dr\,dz\,d\theta$. This integrated power is shown for a case above the power threshold for high-density operation in Fig. 9. The details of the axial deposition are shown in Fig. 10 and can also be inferred from Fig. 5. Figure 9 indicates the parasitic effect of power deposited by evanescent fields in the edge for the high-density mode of operation. Much of the plasma generated by the power deposited in the edge will either be transported radially to the quartz tube or axially along short connection lengths to obstructions in the edge layer.

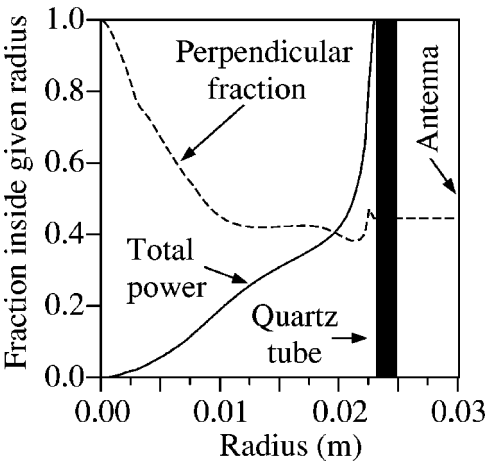

FIG. 9. Roughly half of the coupled rf power is deposited in the evanescent edge region, just inside the quartz tube, and axially localized near the antenna (see also Fig. 5). The case shown here is for 2 kW of total rf power with 700 A in the mirror coil and 56 A in the solenoid (roughly 0.024 T near the antenna).

Also from Fig. 9, the deposition caused by parallel plasma currents accounts for more than half of the total rf power coupled by the antenna, indicating the importance of keeping the parallel field components in the model. Power dissipated near the axis by the perpendicular components of the plasma current must come from the helicon wave. Perpendicular fields also contribute to absorption in a very thin layer near the surface of the quartz tube. Typically for the parameters studied here, we find that, depending on the configuration, from ~40% to ~70% of the power can be deposited by the dissipation of parallel plasma currents in long-wavelength modes or evanescent fields. We also find that relatively little power is dissipated by short-wavelength electrostatic modes because these tend to occur in regions of relatively low plasma density.

A comparison of the axial power and density profiles from the model for three magnetic field cases with contours of the lower hybrid resonance is shown in Fig. 10. These cases correspond to those shown in Fig. 7 for 3 kW of power delivered to the plasma. All of these cases are above the power threshold for high-density operation, and the lower hybrid resonance appears beneath the antenna in the case with 700 A and 56 A in the mirror and solenoid coils, respectively. The axial density profiles are averaged along a radial cord to simulate results that might be measured by an interferometer. Note that the power deposition on axis from the helicon mode is not affected by the location of the lower hybrid resonance. However, the threshold to achieve the high-density mode of operation does appear to be affected by the presence of the lower hybrid resonance near the antenna as shown in Fig. 7.

The model is consistent with the experimentally observed window for operation near the lower hybrid resonance when using hydrogen in Mini-RFTF. The use of heavier gases in the model leads to increased axial confinement times proportional to the square root of the ion mass, which would significantly reduce the power threshold for achieving peaked, high-density operation. More investigation is needed to determine the detailed effects caused by the lower hybrid resonance. However, these results from the model indicate that the presence of the lower hybrid resonance in the low density layer directly beneath the antenna may influence the parasitic coupling to the edge for high density operation. In general, increasing the magnetic field increases the radial confinement and density of the device, but the presence of a lower hybrid resonance in the near-field region of the antenna can increase the power coupled to the edge, thereby reducing the power available to the centrally damped helicon mode. Thus, the presence of a lower hybrid resonance in the antenna near-field region can raise the power threshold for high-density operation, although the details of the process may be complicated by ponderomotive expulsion of plasma in the near-field region. Significant variation in the geometry

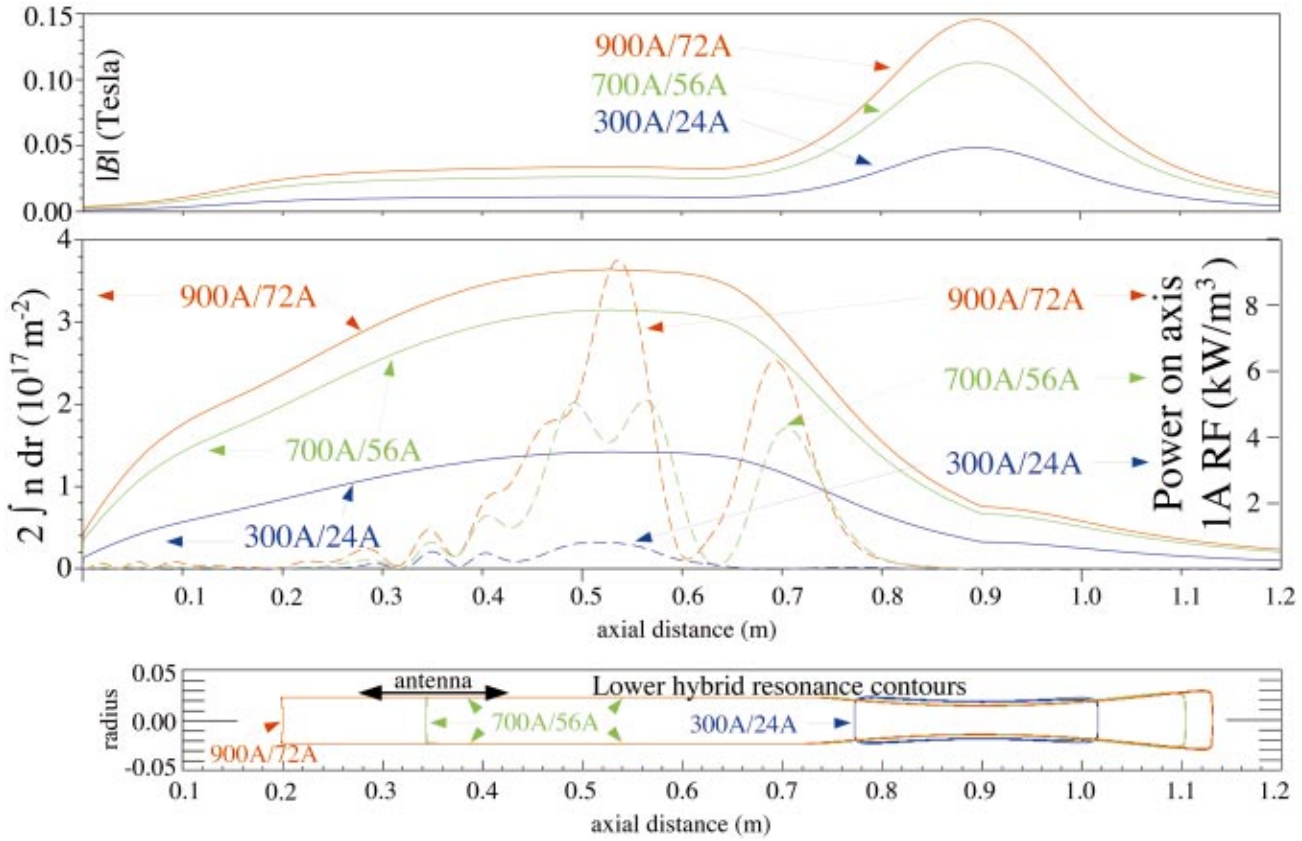

FIG. 10. (Color) The axial variation of the line-averaged density and the power deposition on axis is shown for three different magnetic field strengths all having the same flux tube geometry. The axial variation in the density is determined in the model by the flux-tube-averaged power and transport. The power deposition on axis, caused by collisional damping of the helicon mode, is not sensitive to the location of the lower hybrid resonance. However, the power threshold to achieve peaked high-density operation is sensitive to the location of the lower hybrid resonance. The scale for power deposition is based on an rf current of 1 A in each antenna. The line-averaged density is determined from iterating the model to convergence with 3 kW of power delivered to the plasma for all cases.

of the experiment may be required to isolate effects caused by the lower hybrid resonance from those caused by transport and nonlinear processes.

D. Cavity effects and loading

Cavity effects can significantly influence the operation of systems with damping lengths larger than the size of the cavity, and both traveling waves and eigenmodes consistent with Eq. (1) have been observed in rf wave measurements in helicons.[8,4] Nisoa,[16] for example, has used a carefully constructed system with nearly uniform axial parameters to study the effects of eigenmodes on damping. However, for nonuniform systems, an accurate model must consider the inhomogeneities that can alter these eigenmodes. For systems with strong axial variations,[1,6] the primary factors in determining this eigenmode behavior are the axial magnetic geometry and the resulting plasma itself.

Earlier modeling attempts that neglected parallel rf electric fields[32] indicated that cavity effects could play a role in the Mini-RFTF. However, strong cavity effects on the rf loading are not evident in the typical experimental operation for Mini-RFTF, and no strong evidence is found for them in the EMIR3 modeling results described here. Thus, we find that adding the parallel rf electric field to the rf model strongly buffers cavity effects in the Mini-RFTF device by providing an alternate absorption mechanism. This alternate absorption is predominantly inductive heating very near the antenna.

The antenna coupling (loading) in the model remains a surprisingly weak function of power despite the vastly different densities obtained for different rf powers. The power delivered to the plasma normalized to 1 Amp (peak in time) of rf current for different powers below and above the power threshold are shown in Fig. 11. Variations in capacitor set-

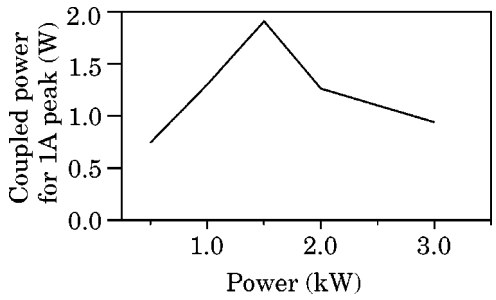

FIG. 11. Real power coupled by the antenna for rf currents of 1 A, peak in time, is calculated by the EMIR3 code. The loading remains surprisingly invariant with density changes below and above the power threshold. Experimental loading values were not measured, but estimates based on capacitor positions indicate loading variations of roughly a factor of 2 and are not inconsistent with the model results.

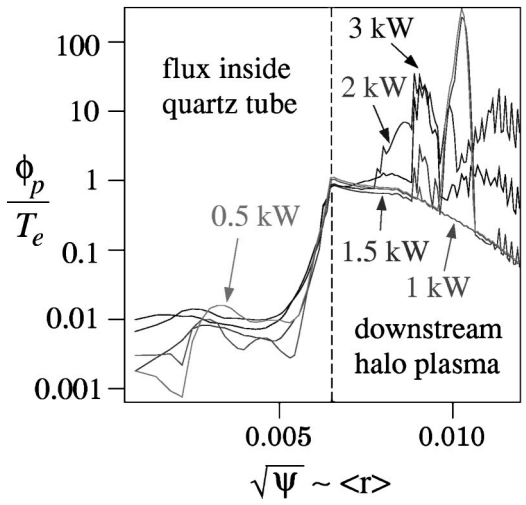

FIG. 12. The maximum estimate for the ponderomotive potential becomes negligible for high-density operation, except near the plasma edge. Very high ponderomotive potentials may be possible in the downstream halo region.

tings for the experiment required to maintain the match indicate that the loading changes by less than a factor of 2, consistent with the modeling results. Variations in the reactive loading are less than 20% in the model results.

The dip in the power deposition on axis near 0.6 m in Fig. 10 may be caused by a transition in the radial mode structure of the helicon wave as shown in Fig. 5. This transition appears to be caused by geometric effects and axial variations in the cavity; however, further work is required to verify that cavity effects are playing a role.

E. Ponderomotive effects

Figure 12 gives the modeling results for the maximum ponderomotive potential on a flux tube for various powers with 700 A and 56 A, respectively, in the mirror and solenoid coils. As shown in Fig. 12, the ponderomotive potential can become comparable with the electron temperature (assumed to be 5 eV in all simulations) near the edge of the discharge at $\sqrt{\psi}\approx 0.006$. The dominant contribution to the parallel electric field inside the quartz tube is from evanescent fields that are axially localized near the antenna. In comparisons (not shown) between cases with $\alpha_p=0$ and $\alpha_p=1$, we find that the ponderomotive potential only weakly affects the power threshold to reach the high-density mode, and it is not important in the high-density central region above the power threshold. However, in some geometries, it may be significant near the plasma edge. These results indicate that a better method for estimating the role of the ponderomotive potential would be useful for understanding phenomena in the discharge.

The ponderomotive force may play an interesting role downstream from the quartz tube. In this region, radial diffusion allows a halo of plasma to form around the main discharge. The power deposited in the downstream halo plasma is typically a small fraction of the total coupled power as shown in Fig. 8, but large parallel fields can be generated by electrostatic waves in this region. Using the field amplitude information from the model, as shown for example in Fig. 5, one sees that rf waves propagating downstream from the quartz tube can excite large parallel electric fields in this low-density halo plasma near the lower hybrid resonance (axially between 0.75 and 0.95 m in Fig. 5). Although the ponderomotive calculation used in this model is far too primitive to accurately estimate the change in potential caused by these fields, it does indicate that enhancements in the potential in the low-density halo plasma could be an order of magnitude larger than potentials found in the main column. These enhanced potentials could give rise to a small number of high energy ions generated in the downstream halo, as are observed in the sister facility to Mini-RFTF located at the Advanced Space Propulsion Laboratory; however, more work is necessary to verify such a mechanism.

VI. CONCLUSIONS

Several methods for producing high-density discharges ($>10^{18}$ m^{-3}) have been found in the Mini-RFTF facility. To date, most of these methods were discovered empirically based on past experience. In this paper, rf modeling has been used to further explore the operation of this device. This modeling work represents an initial attempt to simulate plasmas in the Mini-RFTF device and to compare the results with experiments in hydrogen discharges.

The model includes an accurate rf calculation for cold plasma, including the slow wave, and a simple diffusive transport model. The transport model considers radial and axial diffusion with averages taken along concentric flux tubes and boundary conditions for sonic flow at the ends of each flux tube. Classical electron diffusion in the model shows good agreement with the experiment for the operational regimes considered while radial Bohm diffusion was typically an order of magnitude too large to match the experimental results. From these comparisons and by studying the behavior of the model, we conclude that a soft power threshold to reach high-density operation with peaked profiles in the Mini-RFTF (the helicon mode of operation) is the result of a nonlinear synergism between transport losses, the rf power absorption near the edge, and the propagation and absorption of the helicon wave near the axis.

The synergism in the model arises because of the rf power coupled inductively near the plasma edge and the transport of the plasma in the edge region. Large evanescent parallel electric fields near the antenna can give rise to inductive coupling in a narrow edge layer as c/ω_{pe} becomes small compared with the radius of the device. This power helps to initiate the discharge, but it reduces the efficiency of the device for high-density operation. In the transition to a state with high-density, inductive coupling becomes localized near the edge under the antenna as the power increases, and radial transport allows plasma to diffuse into the center. As the power increases toward the threshold from below, the density increases and begins to isolate the region of high parallel electric fields in the edge region where plasma is lost rapidly by classical electron radial diffusion. However, with sufficient power, the inductive layer becomes thin and the density becomes high enough to begin supporting a colli-

sionally damped helicon mode. The helicon mode damps near the axis because of the radial mode structure of the helicon wave. The increasing density further screens the parallel electric fields in the edge, reducing the radial range of the edge damping and further reducing the fractional power deposition near the edge. Thus, the plasma profile in the model shifts from one that is flat or even hollow at low powers to one that is highly peaked above the power threshold. The presence of the finite-density lower hybrid resonance in the near field region of the antenna may influence the edge damping and modify the power threshold.

The power threshold depends on collisionality and increases with increasing magnetic field. In the model, radial diffusion dominates operation at low magnetic field strengths, allowing sufficient plasma to reach the center and support the helicon mode near the axis at lower power levels than are required for higher magnetic field operation. However, the maximum achievable density at a given power level is lower for low rather than for high magnetic field operation because of the larger radial diffusive losses. At high magnetic fields, axial losses begin to dominate radial diffusion so that plasma formed by inductively coupled power in the edge has more difficulty diffusing inward to support the helicon mode.

The model indicates that power losses in the plasma edge, through inductive coupling mechanisms near the antenna, can become parasitic to the helicon's operation at high-density and high magnetic field. Again, this inductive coupling at the edge may be affected when the lower hybrid resonance is located in the edge near the antenna. The lower hybrid resonance may also play a role in the time evolution of the discharge to the final high-density helicon state. More work to investigate the precise effects of the lower hybrid resonance and the plasma behavior in the near-field region of the antenna is needed.

The model indicates that the ponderomotive force can become significant near the edge of the plasma and downstream from the discharge, where a lower hybrid resonance typically exists. The details of the self-consistent electrostatic potential are beyond the scope of the model used here. However, this simple model indicates that a low-density halo region downstream from the quartz discharge tube could produce high plasma potentials with the possible production of high ion energies for some modes of operation. Additional modeling effort and experimental measurements are required to further investigate this possibility.

More work is also required to determine how far the present model can be extended into other parameter regimes, and what improvements are necessary to accurately simulate the experiment in those regimes. The following possible future refinements to the model may further improve the comparison with experimental results: a consistent electron temperature calculation including radiation losses; a consistent model for the neutral density; a fully two-dimensional transport calculation; and a better calculation of the plasma potential, including ponderomotive effects. Further diagnostics are also needed to spectrally analyze the field results from the EMIR3 code for rf powers below and near the power threshold. Additional efforts should also consider startup scenarios with power deposition near resonance cones as described in Refs. 11 and 23. Additional experimental work for the comparison would include careful neutral pressure scans, measurements of the electron temperature, and possible spectroscopic measurements of the neutral species inside the plasma.

ACKNOWLEDGMENTS

The authors would like to thank Ed D'Azevedo, a member of the U.S. Department of Energy Office of Fusion Energy Science's SCIDAC effort on rf waves in plasmas, for recognizing a matrix restructuring that sped the EMIR3 code up by almost a factor of 10.

Research was sponsored in part by Oak Ridge National Laboratory, managed by UT-Battelle, LLC, under Contract No. DE-AC05-00OR22725, and by Oak Ridge Associated Universities under Contract No. DE-AC05-00OR22750 with the U.S. Department of Energy. Research was also sponsored in part under Contract No. 2044-AA18-Y1 with the National Aeronautics and Space Administration.

[1] F. R. Chang-Díaz, J. P. Squire, A. V. Ilin *et al.*, *Proceedings of the International Conference on Electromagnetics in Advanced Applications (ICEAA 99), Torino, Italy, 1999* (Litografia Geda, Torino, 1999), p. 99.
[2] F. R. Chang-Díaz, Sci. Am. **280** (11), 90 (2000).
[3] H. Takeno, Y. Yasaka, O. Sakai, and R. Itatani, Nucl. Fusion **35**, 75 (1995).
[4] S. Shinohara, N. Kaneda, and Y. Kawai, Thin Solid Films **316**, 139 (1998).
[5] R. L. Miller, T. Ohkawa, S. F. Agnew, B. P. Cluggish, R. L. Freeman, J. Gilleland, S. Putvinski, L. Sevier, and K. R. Umstadter, ''The Archimedes Plasma Mass Filter,'' Bulletin of the 43rd Annual Meeting of the American Physical Society Division of Plasma Physics, Long Beach, CA, KP1.051 2001.
[6] R. H. Goulding, D. Pavarin, F. Angrilli, G. C. Barber, M. D. Carter, R. Maggiora, and D. O. Sparks, *Proceedings of the International Conference on Electromagnetics in Advanced Applications (ICEAA 99), Torino, Italy, 1999* (Litografia Geda, Torino, 1999), p. 107.
[7] W. P. Allis, S. J. Buchsbaum, and A. Bers, *Waves in Anisotropic Plasmas* (MIT Press, Cambridge, MA, 1963).
[8] K. Chi, T. E. Sheridan, and R. W. Boswell, Plasma Sources Sci. Technol. **8**, 421 (1999).
[9] T. Shoji, Y. Sakawa, S. Nakazawa, K. Kadota, and T. Sato, Plasma Sources Sci. Technol. **2**, 5 (1993).
[10] Y. Sakawa, N. Koshikawa, and T. Shoji, Plasma Sources Sci. Technol. **6**, 96 (1997).
[11] Y. Sakawa, T. Takino, and T. Shoji, Phys. Plasmas **6**, 4759 (1999).
[12] A. R. Ellingboe and R. W. Boswell, Phys. Plasmas **3**, 2797 (1996).
[13] Y. Sakawa, T. Takino, and T. Shoji, Appl. Phys. Lett. **73**, 1643 (1998).
[14] K. P. Shamrai, Plasma Sources Sci. Technol. **7**, 499 (1998).
[15] P. A. Keiter, E. E. Scime, and M. M. Balkey, Phys. Plasmas **4**, 2741 (1997).
[16] M. Nisoa, Y. Sakawa, and T. Shoji, Jpn. J. Appl. Phys., Part 1 **40**, 3396 (2001).
[17] Y. Yasaka and Y. Hara, Jpn. J. Appl. Phys., Part 1 **33**, 5950 (1994).
[18] F. F. Chen, Phys. Plasmas **3**, 1783 (1996).
[19] T. H. Stix, *Waves in Plasmas* (American Institute of Physics, New York, 1992).
[20] M. M. Balkey, R. F. Boivin, P. A. Keiter, J. L. Kline, and E. E. Scime, Plasma Sources Sci. Technol. **10**, 284 (2001).
[21] S. Cho, Phys. Plasmas **7**, 417 (2000).
[22] J. L. Kline, E. E. Scime, R. F. Boivin, A. M. Keesee, X. Sun, and V. S. Mikhailenko, Phys. Rev. Lett. **88**, 195002 (2002).
[23] T. H. Stix, *Waves in Plasmas* (American Institute of Physics, New York, 1992), p. 142.
[24] R. W. Boswell and F. F. Chen, IEEE Trans. Plasma Sci. **25**, 1229 (1997).
[25] F. F. Chen and D. D. Blackwell, Phys. Rev. Lett. **82**, 2677 (1999).
[26] F. F. Chen and R. W. Boswell, IEEE Trans. Plasma Sci. **25**, 1245 (1997).

[27]S. Yun, J. Kim, and H. Chang, J. Vac. Sci. Technol. A **15**, 673 (1997).
[28]K. P. Shamrai and V. B. Taranov, Plasma Sources Sci. Technol. **5**, 474 (1996).
[29]E. E. Scime, P. A. Keiter, M. W. Zintl, M. M. Balkey, J. L. Kline, and M. E. Koepke, Plasma Sources Sci. Technol. **7**, 186 (1998).
[30]D. L. Book, *NRL Plasma Formulary* (Laboratory for Computational Physics and Fluid Dynamics, Naval Research Laboratory, Washington, DC, 1987).
[31]M. Light, F. F. Chen, and P. L. Colestock, Phys. Plasmas **8**, 4675 (2001).
[32]M. D. Carter, F. W. Baity, Jr., R. H. Goulding, E. F. Jaeger, F. R. Chang-Díaz, and J. P. Squire, *14th Top. Conf. on Radio Frequency Power in Plasmas*, Oxnard, CA, AIP Conf. Proc. 595 (American Institute of Physics, New York, 2001), p. 465.
[33]*American Institute of Physics Handbook*, 3rd ed., edited by D. E. Gray (McGraw-Hill, New York, 1972), pp. 8–184.
[34]P. Clark Souers, *Hydrogen Properties for Fusion Energy* (University of California Press, Berkeley, 1986), p. 234.